IEEE Access
Multidisciplinary ⋮ Rapid Review ⋮ Open Access Journal

Received 2 September 2022, accepted 9 October 2022, date of publication 13 October 2022, date of current version 20 October 2022.

Digital Object Identifier 10.1109/ACCESS.2022.3214526

APPLIED RESEARCH

Quasi-Resonant Flyback Converter as Auxiliary Power-Supply of an 800 V Inductive-Charging System for Electric Vehicles

DARKO Đ. VRAČAR, (Member, IEEE)
School of Electrical Engineering, University of Belgrade, 11000 Belgrade, Serbia
BRUSA Elektronik (München) GmbH, 81829 Munich, Germany

e-mail: darko.vracar@brusa.biz

This work was supported by BRUSA Elektronik (München) GmbH, Munich, Germany (www.brusa.biz).

ABSTRACT This paper presents evaluation of quasi-resonant flyback (QRF) dc-dc converter 57 W with valley-switching in an emerging application. The QRF was supplied from an 800 V variable dc-link and was used as the auxiliary power-supply of a wireless inductive-charging system (ICS). Comparison of state-of-the-art QRF control ICs is presented and suggestions for their improvements are given. Notes on the power-supply architecture, design items specific for the ICS application, over-power protection, and key-component choice are provided. During experiments several original and novel results are generated. The QRF efficiency graphs in ICS power transfer, ICS stand-by, and constant-load operation are analyzed. The maximum efficiency of 87.1% was reached at 620 V and rated load. Moreover, the unique analysis of QRF losses at no-load, showed their quadratic dependency vs. input-voltage. The measured "*switching frequency vs. load*" graph is presented. It was changeable with load and input-voltage as expected. From Bode plots the bandwidth, phase-margin, and gain-margin are extracted and plotted versus input-power—for the first time. They were changeable with input-voltage and load as expected. Comparison of simulated and measured Bode plots showed that, even when they were not matched, one can still design a Type-2 compensator that ensures stable operation. Evaluation of cross-regulation, when output with 24.1% of total power was regulated, showed that such approach—contrary to the more common of regulating the biggest one—is feasible too. It is discovered that, for a QRF with variable switching frequency, choice of compensator's zero or the regulated output has influence on its efficiency. The power-thresholds, to ensure valley-switching operation, represented as "*input power vs. input voltage*" are shown for the first time. Comparison of bandwidth, phase margin, and gain margin vs. input power, between an active-clamped flyback (ACF) and the QRF converters, were discussed. Conclusion is that QRF, for the same specification, cannot have the same compensator as an ACF or conventional flyback dc-dc converter. The difference must be at least in a placement of a zero.

INDEX TERMS Active-clamped flyback, Bode plots, control, cross-regulation, dc-dc converter, efficiency change, over-power protection, quasi-resonant flyback, switching-frequency change.

NOMENCLATURE

ACF	Active-clamped flyback.
APS	Auxiliary-power supply.
BEV	Battery electric-vehicle.
DCM	Discontinuous-conduction mode.
HDCIV	Higher-dc-input-voltage.
IC	Integrated circuit.
ICS	Inductive charging-system.
OPP	Over-power protection.
QRF	Quasi-resonant flyback.
RCD	Resistor-capacitor-diode.
SiC	Silicon-carbide.
SMD	Surface-mounted device.
VSM	Valley-switching mode.
ZCD	Zero-crossing detection.

The associate editor coordinating the review of this manuscript and approving it for publication was Subrata Banerjee.

I. INTRODUCTION

As battery electric-vehicles (BEV) are becoming more popular [1] so it is research about wireless inductive-charging of their batteries [2] or market studies [3]. By reviewing relevant literature it was noticed that research focus was mainly on power-conversion, efficiency improvements, compensation techniques, control, coil design, protection, etc. [2], [4]. To our best knowledge the auxiliary power-supplies (APS) of such systems did not receive attention except in [4], [5], [6], and [7]. In those papers the active-clamped flyback (ACF) dc-dc converter was used as an APS of the primary (i.e. ground) side of an inductive-charging system (ICS) for charging of battery electric-vehicles.

In those papers the APS was supplied with higher-dc-input-voltage (HDCIV) compared to a typical ACF application (i.e. from rectified single-phase universal grid). Hence, the term HDCIV was introduced in [4] referring to input dc voltages higher than >450 V and lower than 1500 V to avoid confusion with term high-voltage (HV) defined per standard [8]. But, in automotive-sector the term high-voltage denotes voltages > 60 V and ≤ 1500 V (dc) and > 30 V and ≤ 1000 V (ac rms) per [9]. Note that the term ICS is used in *BRUSA Elektronik AG*, instead of (wireless) inductive power-transfer (IPT) system. Hence, it will be used here too.

In this study we will investigate design, operation, and challenges when the quasi-resonant flyback (QRF) dc-dc converter 57 W, with valley-switching mode (VSM), is used as an APS in an emerging HDCIV application, i.e. ICS. The variable-frequency valley-switching QRF converter is a well-known topology since a long time [10], [11]. In further text it will be referred as QRF or QRF with VSM. Its typical application is either as a power adapter [12] or auxiliary (i.e. housekeeping) power supply [13], [14] of various products. The QRF general analysis, operation, and design are explained in [15], [16], [17], [18], [19], and [20]. Some methods for noise-free and valley-locking operation are covered in [21] and [22]. Hence, readers are advised to check those references for more information.

General advantages of any variant of flyback converter, except for an ACF, are simplicity, low-cost, ease of isolation, and having multiple-outputs. General disadvantages, except for an ACF, are that they have poor efficiency and high electro-magnetic interference.

The generic schematic of a QRF with valley-switching is shown in Fig. 1. We see that, from topology viewpoint it is not different from the conventional flyback dc-dc converter. A QRF with VSM is different in a sense that a circuit, which senses voltage of auxiliary primary-winding (V_{aux}), is introduced. Purpose of that circuit is to detect zero-crossing of the switch Q drain-voltage, i.e. the instant when energy from transformer is depleted. After that, a signal for turn-on of the switch Q is given ensuring valley-switching thus reducing switching losses and improving efficiency. The SN in Fig. 1 denotes switching node which is equal to the drain-source voltage of the switch Q. A typical

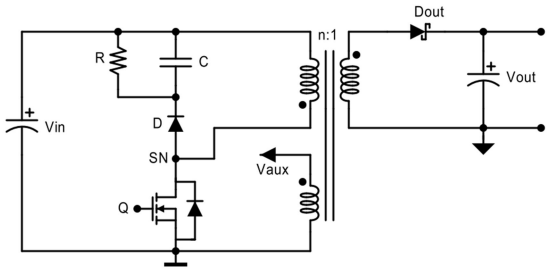

FIGURE 1. The QRF generic schematics with one output.

QRF application circuit is shown in [23] (*Figure 2* on the *page 2*).

Motivation of writing this paper was to share theoretical considerations, simulation, and experimental results for the 57 W QRF in ICS application and compare it with the previous work for an ACF with the same specification and application. A comprehensive study of the 57 W ACF in an 800 V ICS was presented in [4] and its companion [7]. Note that this paper introduces neither a new topology nor a control strategy but presents usage of the known topology (QRF with VSM) in an emerging HDCIV application (i.e. ICS for BEV). However, the conclusions presented here are valid for a QRF in any application. Moreover, a balance between practical and academic contributions is tried to be achieved in this paper thus making it useful for both industry and academia.

Note that critical analysis of many references will be done on-the-fly throughout the paper—not in this section. In addition, this study is part of a commercial project hence not all technical details will be revealed—only minimum will be provided to support the claims and key-contributions.

A. PAPER CONTRIBUTIONS

During literature review (> 70 papers) several gaps were identified. The original or novel contributions are listed below.

- Comparison of state-of-the-art QRF analog control ICs presented. Suggestions for improvements are given and are supposed to motivate vendors to develop new devices that are targeting HDCIV applications.
- Power-supply architecture of an APS in ICS analyzed. It was shown that single-stage approach requires less space and is much cheaper—although higher efficiency might be achieved with two dc-dc stages in cascade.
- The converter and transformer data are presented. Short notes given on items that are specific for the ICS application and key-component choice is explained.
- Over-power protection (OPP) was analyzed, and guide given for the key-part choice in its circuit.
- Operational waveforms are simulated and measured showing that voltages and primary currents had some acceptable deviations. For example, at 850 V operation

there was mismatch between simulated and measured switching-valley for the switch turn-on.

- The QRF efficiency graphs in ICS power transfer, ICS stand-by, and constant-load operation presented and analyzed. The maximum efficiency of 87.1% was reached at 620 V and rated load. The efficiencies of QRF are higher than ACF, as expected, due to absence of circulation-energy losses, and a lower switching-frequency for the same load and input voltage.
- Unique graph of QRF losses at no-load is analyzed showing quadratic dependency of losses vs. input dc voltage.
- The "*switching-frequency vs. load*" and "*drain-source voltage of switch vs. load*" graphs are presented for the first time for a QRF in an 800 V system. As expected, both were changeable with load and input-voltage.
- Bode plots are measured for two input-voltages and at 10 different loads. Then bandwidth (f_c), phase-margin (PM), and gain-margin (GM) are extracted and plotted versus input-power—for the first time. They were changeable with input-voltage and load as expected. In addition, from those plots one can confirm that with only Type-2 compensator (integrator, one pole, and one zero) the QRF converter can be stabilized. In other words, there was no need to go for Type-3 compensator (i.e. dc gain, two poles, two zeros, and integrator). The simulated and measured dynamic-load (i.e. step-load) change graphs are shown to verify this approach.
- Comparison of simulated and measured Bode plots of QRF at 620 V and 850 V inputs with rated load demonstrated that, although they were not well matched, one could design a compensator that ensures stable operation over input-voltage and load ranges—which was experimentally verified. In other words, the simulation helped to notice directions of changes during the design process hence to ensure design of a good compensator. And that is what counts in practice.
- Cross-regulation of the QRF with five outputs is elaborated in a case where regulated output was the one with 24.1% of the total power. This was contrary to the common approach of regulating the output with highest power (i.e. 67.1% in our case). In addition, those results were compared to the ACF in the same application, with the same transformer, showing similar pattern except for the non-regulated 5.5 V output.
- It was shown that, for a QRF with variable switching frequency, choice of compensator's zero or regulated output has influence on its efficiency.
- The power-thresholds, to ensure that QRF enters into VSM operation, represented as an "*input power vs. input voltage*" are shown for the first time.
- Comparison of Bode plots for ACF and QRF converters is presented for the first time too. It was shown that, for the same specification, ACF and QRF cannot have the same compensator. The difference must be at least in placement of a zero.

II. DESIGN NOTES

The design considerations for the power stage such as primary switch, transformer, output capacitors, and output rectifiers are similar as for any conventional flyback dc-dc converter hence will be omitted [4]. Only specific aspects of the QRF in ICS application will be elaborated here.

A. OVERVIEW OF QRF CONTROL ICs

For an APS of any power-electronic system (PES) a dedicated analog control IC is needed to make possible that it can operate standalone. The APS has to start during PES power-on and operate reliably in all operating conditions for the PES designed lifetime. The APS efficiency per se is not the key parameter as long as there are no thermal-related problems [4]. The flyback dc-dc converter (in all variants) is typical and most popular dc-dc converter for an APS.

The key-criteria for choice of a QRF control IC were that it has integrated HV start-up circuit ≥700 V, valley lock-out, and that simulation model in SIMPLIS [24] was available. Rest of the features of interest is covered in Table 1 together with comparison of several off-the-shelf control ICs [23], [25], [26]. Note that for the QRF in HDCIV application there were many ICs to choose from—contrary to the ACF case [4]. But not all could have been included into our analysis—only best candidates are presented in the Table 1. Based on criteria from the Table 1 the NCP1340 (9-pin variant with manual setting of the maximum switching-frequency) [23] was chosen as the control IC for our application. An interesting product for QRF control with integrated 1700 V MOSFET appeared on the market recently [27], but that was too late for this study. Anyway, that product is intended for use with synchronous rectification—which is not our case.

TABLE 1. Overview of some QRF control ICs.

Item/Manufacturer	*onsemi* [23]	*TI* [25]	*ST* [26]
Part number	NCP1340	UCC28600	L6566BH
HV start-up ≥ 700 V (built-in)	yes	**no**	yes
Enable signal	no	no	yes
Valley-lockout feature	yes	**no**	**no**
Max switching frequency	1 MHz	130 kHz	300 kHz
Frequency jittering	yes	**no**	yes
Adjustable over-power protection	yes	**no**	yes
Adaptive multi-mode operation	yes	yes	yes
Light/no-load management	yes	yes	yes
External gate-driver needed	no	no	no
Adjustable maximum-frequency clamp	yes	**no**	**no**
SIMPLIS model available	yes	yes	**no**
Package	SOIC-8 **SOIC-9**	SOIC-8	**SO-16N**

After testing of the QRF following suggestion of features for future QRF control ICs targeting HDCIV systems are:

- HV start-up and self-supply to be in 240–950 V dc input voltage range. That would save costs, board-space and design-effort.
- Manual setting of the maximum switching frequency to be in the range of 60–130 kHz.
- Manual adjustments of the over-power protection (OPP) level.
- Stable and noise-free operation of valley lock-out in the whole input-voltage and load ranges. Although it was claimed that this feature exist—in some specific operating points the opposite effects still may be noticed. The reason for deviation might be that the HDCIV application was not the intended one when designing a QRF control IC.
- *Optional:* Availability of advanced simulation models (e.g. in SIMPLIS [24]) for both transient and ac simulations.

B. POWER-SUPPLY ARCHITECTURE

The APS was connected to the variable dc-link as shown in Fig. 2—which is typical for industrial applications [7]. Note that in [6] the ACF was supplied directly from rectified three-phase grid—which belonged to the HDCIV system as well. But that concept was abandoned due to requirements to withstand surge-voltage tests per [28]. The two evaluated architectures of APS, with input from the dc link, are shown in Fig. 3. In our case, the single-stage variant (a) was used due to board-space constraints. However, the two-stage variant (b) could give benefits in increased APS efficiency, easier and cheaper design of the QRF including its transformer. However, in that case one would have to take care of HV start-up of the first dc-dc (non-isolated) converter thus increasing overall complexity and occupied board-area.

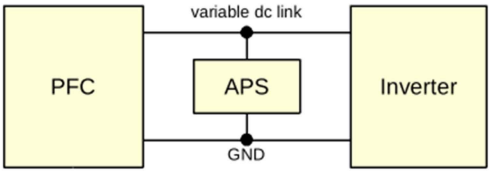

FIGURE 2. The APS connection-point in the ICS.

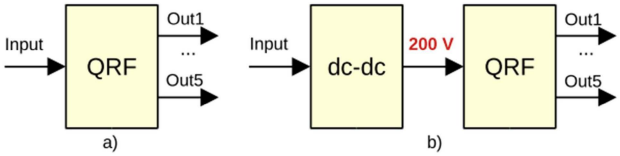

FIGURE 3. Possible power-supply architectures for the APS in ICS: a) single stage, b) two stages in cascade.

C. CONVERTER DATA AND CHALLENGES

The specification of the 57 W QRF is given in Table 2. It is slightly different to the ACF in [4], [5], and [7] in a sense that the QRF had limited maximum switching frequency and much lower minimum input voltage. That enabled QRF to operate with all possible three-phase and split-phase input ac voltage ranges worldwide including respective min/max tolerances. Moreover, loads between outputs 1 and 2 are redistributed a bit, but total power remained the same (57 W). Hence, the regulation in this study is done on the Output 2 (24.1% of the total power).

TABLE 2. The 57 W QRF Specification.

Parameter	Value
Input dc voltage (ICS power transfer)	620–880 V
Input dc voltage (ICS stand-by)	240–640 V
Output 1: voltage	+ 5.5 V
Output 1: load current	0.7 A
Output 2: (regulated) voltage	+ 5.5 V
Output 2: load current	2.5 A
Output 3: voltage	+ 22 V
Output 3: load current	1.74 A
Output 4/5: voltage	± 11 V
Output 4/5: load current	± 40 mA
System stand-by power	< 10 W
Minimum duty-cycle	9.0%
Maximum duty-cycle	26.6%
DC voltage-conversion-ratio at 5.5 V	43.6–154.5
Maximum switching frequency, f_{sw_max}	67 kHz

The QRF has two input-voltage ranges: the ICS power-transfer mode and the ICS stand-by mode. This was one of the challenges specific to the ICS application in general [4], [5], [7]. In ICS stand-by mode and loads less than 30–35 W, this QRF operated either in the skip-mode [23] or in the discontinuous-conduction mode (DCM) like a conventional flyback dc-dc converter in order to increase the efficiency. With higher loads, the QRF was operating in the VSM—which is expected in the ICS power-transfer mode.

The used control IC was *onsemi* NCP1340 quasi-resonant multi-mode controller with valley lock-out switching [23]. Additional application-notes [29], [30], [31], for other control ICs, were helpful during the design and readers shall check them. The maximum switching frequency of 67 kHz was set by external resistor 390 kΩ (pin 2: *FMAX*) [23] to make comparison with the ACF from [4] and [7] easier.

Since input dc voltage with ripple was approaching 880 V in normal operation one had to use the same SiC FET 1700 V [32] as a power switch like in [4], [5], and [7]. That also eased comparison with the ACF 57 W in those papers. But this power switch is a single-source part—which is not preferred for the mass-production.

Additional challenge was choice of the snubber diode. Ideally such a diode shall be in a SMD (smaller) package (e.g. SMA), be rated for minimum 1500 V, have forward voltage-drop <1.65 V, and ultra-fast recovery characteristics. But such a diode still does not exist on the market. Hence, in this design, two 1600 V ones were used in parallel to reduce forward voltage-drop hence losses. Other available

diodes (≥1500 V) were either standard- or fast-recovery ones or with forward voltage-drop in the range 3–6 V—which was not desired.

D. TRANSFORMER DATA

The design of a QRF transformer is similar to any other flyback one. Hence, only few notes will be given here. A comprehensive study on transformer design for a DCM flyback with multiple outputs is presented in [33]. The specification of the transformer 60 W, that was used, is listed in Table 3 with its schematic symbol given in Fig. 4 [7]. It was a bit overdesigned (60 W) to have some reserve if requirements change later. More info about design choices, calculation and measurement of magnetizing inductance one can find in [4]. The auxiliary winding in Fig. 4 provides self-supply of the control IC on the primary side [7]. Note that term transformer will be used here instead of the more suitable "coupled-inductors" for a flyback dc-dc converter because it is widely used in everyday practice.

TABLE 3. Specification of transformer.

Parameter	Value
Maximum primary working voltage	> 960 V
Clearance and creepage distances	> 7.9 mm
Turns ratio primary to output 1 and 2	15
Turns ratio primary to output 3	3.75
Turns ratio primary to output 4 and 5	7.5
Core shape	ETD29
Core material	N87, TP4, DMR40
Magnetizing inductance, L_m	600 µH
Leakage inductance, L_k	< 9 µH
Max peak primary-current, I_{pri_max}	1.82 A

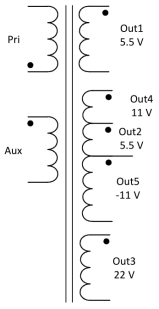

FIGURE 4. The schematic symbol of the transformer T3.

The transformers were designed and built by three vendors per specification in Table 3. A representative photo is given in [7] (*Fig. 4*). They were potted and belong to temperature-class B (130 °Cn). All details of their construction are not known. Anyway, since this is a custom-design such data are normally not allowed to be published. One can assume that differences are coming from different wires and air-gaps used, hence difference in losses as well. Also, from data in Table 3, one can assume max magnetic field density in mT and estimate number of turns by oneself. The safety distances (clearance and creepage) were calculated per [34] and [35].

TABLE 4. Overview of the used transformers.

Transformer: L_m, vendor	n_{eff}
T3-1: 600 µH, vendor 1, rev. 1	15.53–15.54
T3-2: 600 µH, vendor 2	13.65
T3-3: 600 µH, vendor 3	14.81–15.54
T3-4: 600 µH, vendor 1, rev. 2	14.96–15.03

In Table 4 a summary of the used transformers is given including effective turns-ratio (n_{eff}). The calculated turns-ratio (primary to the regulated +5.5 V output) was 15. From Table 4 we can see that effective turn-ratios vary in range −9% to +3.6% versus the rated one—which is acceptable. They were calculated as [7]

$$n_{eff} = \sqrt{\frac{L_{m\_meas}}{L_{out1\_meas}}} \tag{1}$$

where L_{m_meas} is the measured magnetizing-inductance and L_{out1_meas} is the measured inductance of the Output 1. Those values were measured with a precision LCR-meter. The leakage inductances of all of them were ≤9 μH and are not included in the Table 4.

E. OVER-POWER PROTECTION

A QRF exhibits wide peak-current variation depending on the input-voltage change [30]. As a consequence, the QRF output-power range increases with increase of the input-voltage [30]. A common way of limiting output-power in such cases is called over-power protection (OPP) [30]. In Fig. 5 one possible solution to it is shown [30] and which is used in this study as well. Moreover, that circuit is also used for the zero-crossing detection (ZCD)—which is necessary for QRF with VSM. In the [30] a detailed design-procedure of that circuit is given as well. Here we will provide only part of it to ease the paper comprehension.

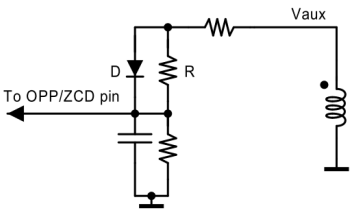

FIGURE 5. The schematic of the ZCD/OPP circuit [30].

The peak-current at high input-voltage is calculated as [30]

$$I_{pkh} = \frac{0.8\,V}{R_S} + V_{in\_\max} \cdot \frac{350\,ns}{L_m} \tag{2}$$

where R_s is the shunt-resistance, 0.8 V is the current-limit threshold-voltage [23], V_{in_max} is maximum (regulated) input

dc voltage (850 V), and 350 ns is the total propagation-delay of the control IC [23]. The switching-period at high input-voltage is calculated as [30]

$$T_{swh} = I_{pkh} \cdot L_m \cdot \left(\frac{1}{V_{in\_\max}} + \frac{1}{n \cdot (V_{out} + V_f)}\right) + \pi \cdot \sqrt{L_m \cdot C_{lump}} \quad (3)$$

where V_f is the forward-voltage drop of output diode, and C_{lump} is the lumped parasitic capacitance at the switching node (165 pF). Rest of the data is provided in Table 2 and Table 3. The high output-power can be found per [30]

$$P_{out\_high} = 0.5 \cdot L_m \cdot I_{pkh}^2 \cdot f_{swh} \cdot \eta \quad (4)$$

where: f_{swh} is the switching-frequency at high input-voltage ($f_{swh} = 1/T_{swh}$) and η is the estimated efficiency. So, for our QRF one gets peak-current of 2.46 A and maximum power of 78.76 W—which is not desirable. Hence, maximum output power in this study was limited to 60.5 W by setting resistor R to 1 MΩ. In order to disable the OPP one can simply change that resistor to some higher value (e.g. 10 MΩ).

Key-component in circuit from Fig. 5 is the diode D. Its purpose is to separate OPP and ZCD action depending on the V_{aux} polarity. It has to be rated for at least 350 V, have low forward-voltage drop and ultra-fast recovery characteristics. Otherwise, its leakage current will influence OPP detection thresholds and cause its premature action (e.g. at 800 V) followed by the QRF restart. Also, choice of this diode is important in the simulation model as well otherwise QRF switching frequency will vary (i.e. oscillate) a lot.

III. SIMULATION RESULTS

The 57 W QRF with 600 μH transformer was simulated in SIMPLIS [24]. Reasons were speed of simulation and availability of the NCP1340 model, but only for transient simulations. Note that internal structure of the NCP1340 model was password protected, i.e. it is not known to users. Standard blocks from SIMPLIS library were used for the QRF model. The total (lumped) parasitic capacitance of the switching node was estimated to be ≈165 pF and was included in the model. Maximum switching-frequency was set to 67 kHz. The leakage inductance (8 μH) was not included in the QRF model since it caused excessive non-plausible ringing of the switch drain-voltage and increased the simulation-time significantly too (e.g. from 61 s to 143 s).

A. OPERATION IN ICS POWER-TRANSFER MODE

The simulation results of gate-source voltage, voltage of zero-crossing detection (ZCD) pin and drain-source voltage (V_{DS}) at 620 V dc input and 57 W are shown in Fig. 6. There one can notice that the valley-switching is working as expected and switch turn-on happens at second valley. The clamped-voltage of switch Q (i.e. SN point) by RCD snubber was ≈719 V. The QRF model was somewhat idealized hence voltage ringing at switch turn-off is not visible. Magnetizing and primary currents are presented in Fig. 7 with peak values of 2.04 A. The switching frequency was 59.58 kHz.

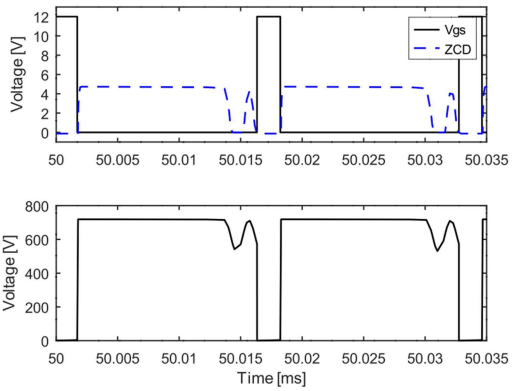

FIGURE 6. The QRF gate, ZCD and drain-source voltages in steady-state at 620 V input and rated load.

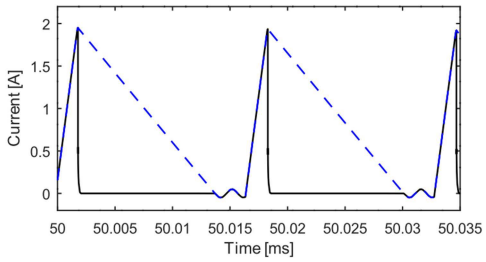

FIGURE 7. The simulated magnetizing (blue dashed line) and primary (black solid line) currents in steady-state at 620 V dc input and rated load.

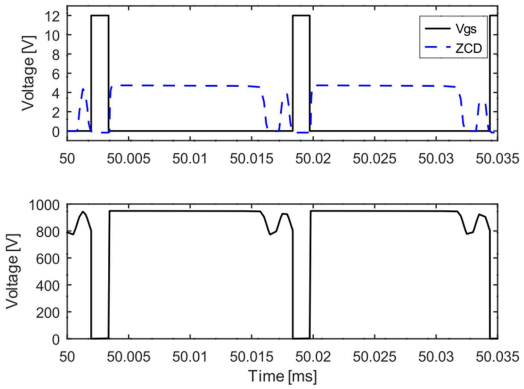

FIGURE 8. The QRF gate, ZCD and drain-source voltages in steady-state at 850 V input and rated load.

Similar waveforms for operation at 850 V dc input and 57 W are shown in Fig. 8. In this case the switch turn-on happens at second valley too. The RCD clamped-voltage of switch was ≈949 V. The magnetizing and primary currents are shown in Fig. 9 with peak values of 2.07 A. The switching frequency was 59.21 kHz, i.e. not much different than in the 620 V case. In experimental section we will see whether that is valid in reality as well.

In both cases the ZCD pin had almost the same maximum voltages (≈4.74 V) as calculated. The negative values for 620 V and 850 V inputs, which determine the OPP

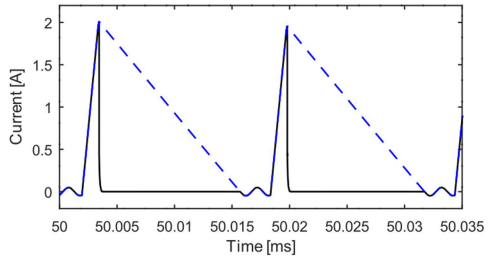

FIGURE 9. The simulated magnetizing (blue dashed line) and primary (black solid line) currents in steady-state at 850 V dc input and rated load.

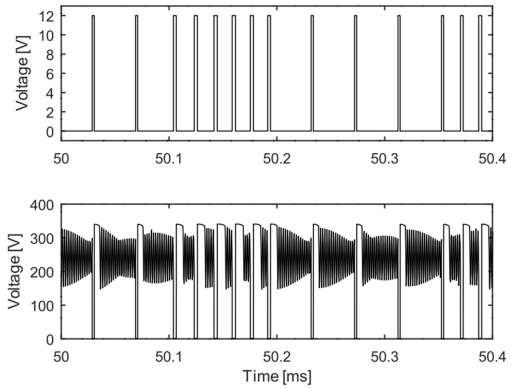

FIGURE 10. The QRF gate and drain-source voltages at 240 V input and stand-by load.

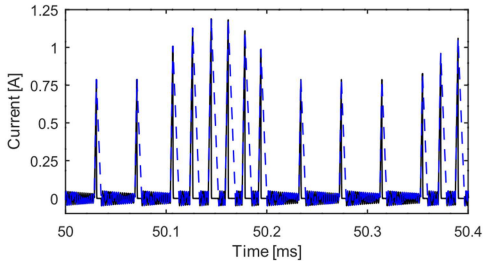

FIGURE 11. The simulated magnetizing (blue dashed line) and primary (black solid line) currents at 240 V dc input and stand-by load.

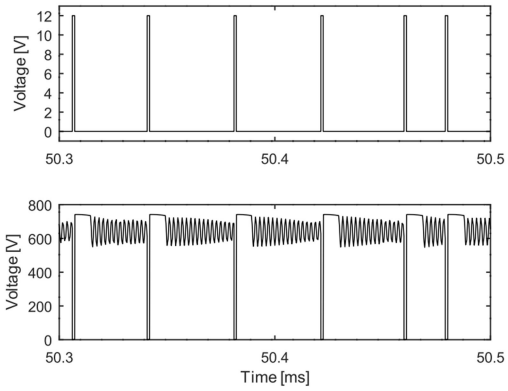

FIGURE 12. The QRF gate and drain-source voltages at 640 V input and stand-by load.

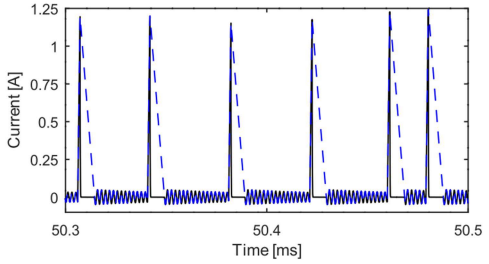

FIGURE 13. The simulated magnetizing (blue dashed line) and primary (black solid line) currents at 640 V dc input and stand-by load.

thresholds, were −125 mV and −171 mV, respectively. They were not constant—as expected.

B. OPERATION IN ICS STAND-BY MODE

In this mode the 22 V output has only bleeder resistors connected and other outputs were having lower loads than in the ICS power-transfer mode. In addition, input voltage range is different than in ICS power-transfer mode (Table 2). The simulation results of gate-source voltage and drain-source voltage (V_{DS}) at 240 V dc input and 10 W are shown in Fig. 10. There one can notice that the QRF is not working in VSM, but rather in DCM with quasi-stable transition between several switching frequencies. Similar, but not so strong, behavior was noticed when operating at 640 V (Fig. 12). In Fig. 11 and Fig. 13 primary and magnetizing currents are presented at 240 V and 640 V, respectively. The peak-current values were changeable following the switching-frequency changes.

Such behavior of NCP1340 is probably result of the internal logic and how controller decides when to initiate the turn-off signal.

C. BODE PLOTS AT 620 V AND 850 V

With SIMPLIS it was very easy and fast (5–6 s) to generate the Bode plots. Unfortunately, the available NCP1340 model from vendor was suitable only for transient simulations, i.e. it operated with variable switching frequency. But for Bode plots one needs constant switching frequency to be able to generate them. Therefore, a generic QRF model from [36] was modified a bit to match properties of the NCP1340. Then it was possible to generate Bode plots. However, that model doesn't have limitation of the maximum switching-frequency, so the resulting ones were 80.3 kHz and 85.9 kHz for operation at 620 V and 850 V, respectively. Also, the settings of parametrized optocoupler in SIMPLIS were adjusted (current transfer-ratio 1.6, 1st pole frequency 4 kHz and output capacitance of 3.07 nF).

In Fig. 14 the Bode plots of overall loop at 620 V and 850 V are shown. Both simulation runs were executed at rated load. The Fig. 14 shows that there is no significant difference between simulated Bode plots in operation at 620 V and 850 V. Whether in reality is similar to that we will find out in the experimental section where detailed findings are summarized in Table 6. Furthermore, in Fig. 14 one can notice

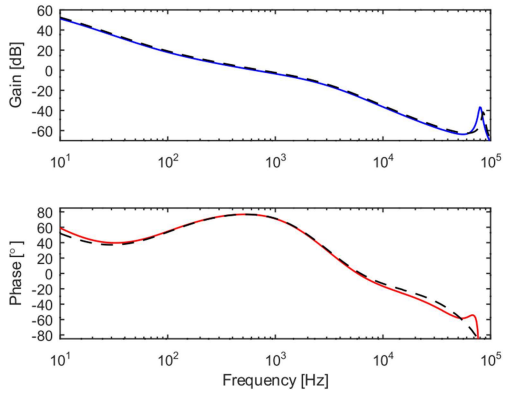

FIGURE 14. The simulated Bode plots at 620 V (blue and red solid lines) and 850 V (black dashed lines) inputs at rated load and valley-switching.

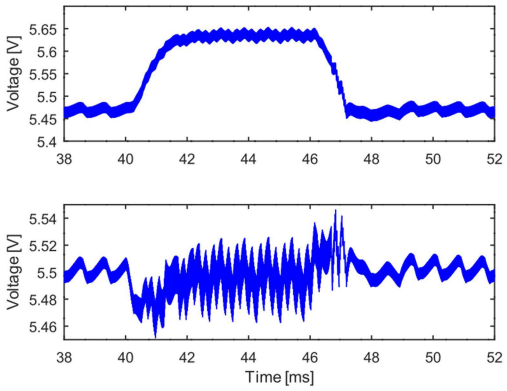

FIGURE 16. The dynamic load-change at 850 V input. Upper trace: non-regulated 5.5 V output with 0.7 A load. Bottom trace: regulated 5.5 V output with load change from 0.5 A to 2.5 A and vice versa.

first-order response, as expected, which is typical for any peak-current controlled flyback dc-dc converter [4], [37].

D. DYNAMIC LOAD CHANGE

The simulation of dynamic load-change at 5.5 V regulated output with 0.5 A→2.5 A→0.5 A at 620 V input is shown in Fig. 15. There it can be noticed that regulator works as expected with minimum deviations of regulated (5.453–5.544 V) and non-regulated (5.451–5.649 V) 5.5 V outputs. In addition, one can see at the regulated output that ripple is higher at higher load, as expected. Note that the non-regulated output (Output 1) has lower value than rated one because that depends on load at the regulated output (i.e. with 0.5 A load current there was not enough gain).

The similar results for test at 850 V are shown in Fig. 16. The regulator worked as expected with minimum deviations of regulated (5.451–5.546 V) and non-regulated (5.444–5.653 V) 5.5 V outputs. We see that those results are very close to the ones for 620 V case, i.e. differences are only at the third digit. One can see that voltages need a bit more time to settle down after current was reduced compared to the 620 V case.

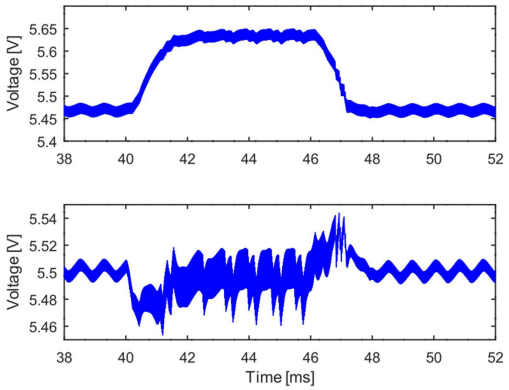

FIGURE 15. The dynamic load-change at 620 V input. Upper trace: non-regulated 5.5 V output with 0.7 A load. Bottom trace: regulated 5.5 V output with load change from 0.5 A to 2.5 A and vice versa.

Note that Output 1 had rated load (0.7 A) and that current change rate at the regulated output was ±2 A/ms in both cases. Other voltages were not shown because they have wider allowed tolerances hence their variations were not critical.

IV. EXPERIMENTAL RESULTS AND DISCUSSION

The QRF, as specified in Table 2, was built and tested. The photo of the prototype-board is given in Fig. 17 [4]. Note that output diodes are not marked, but one shall be able to see them easily.

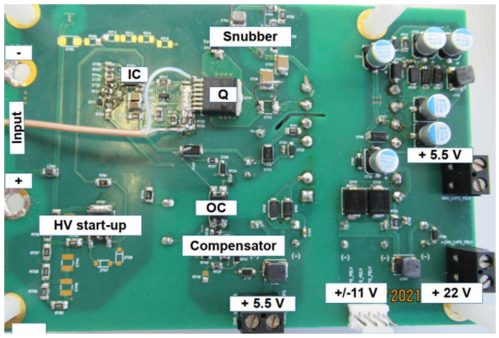

FIGURE 17. Photo of the 57 W QRF prototype-board (top-view) [4].

Tests were done in a way that both 5.5 V and 22 V outputs were loaded by dc-electronic-loads and the ±11 V outputs had only bleeder resistors of 10 kΩ as loads [4]. This was done in order to make testing easier and had no influence on the findings. The dc-supply-voltage was provided by a high-voltage dc-source. Majority of experiments are done with the transformer T3-1 (Table 4) and for exceptions a note will be given.

A. OPERATION IN ICS POWER-TRANSFER MODE

The key waveforms at 620 V and 850 V input voltages and rated loads are presented in Fig. 18 and Fig. 19, respectively. The legend of the oscilloscope waveforms in this subsection and subsection B is as follows: **CH1** (yellow; 1 A/div;

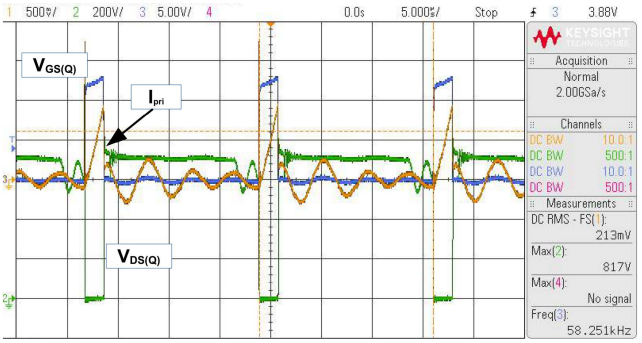

FIGURE 18. The 57 W QRF operating at 620 V dc input and rated load with valley-switching (2nd valley).

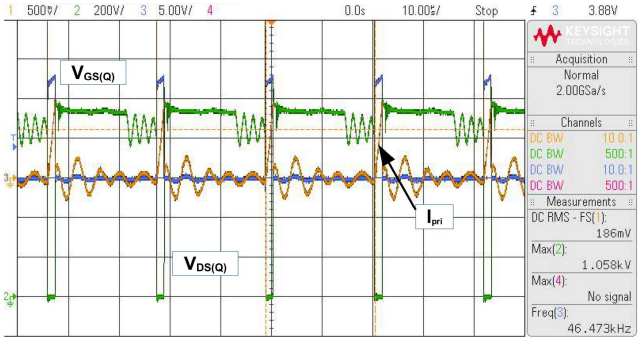

FIGURE 19. The 57 W QRF operating at 850 V dc input and rated load with valley-switching (4th valley).

primary current), **CH2** (green; 200 V/div; drain-source voltage), and **CH3** (blue; 5 V/div; gate-source voltage).

In Table 5 comparison of simulated and measured results at rated load is provided. Only few key-parameters were considered. One can see that the (RCD clamped) drain-source voltages are a bit lower than in simulations (Fig. 6, Fig. 8). And that was good because it is on a side of safety. The opposite case would not be good. In addition, we can wee that the maximum currents on primary side are a lower than the simulated ones—which is good—and they are matched with the calculated one (Table 3). The difference is in the valley-number at which switch turn-on happens at 850 V hence the operating frequency. But that was not a problem because the switching losses were lower. One should have been worried if it were the opposite. Since structure of the NCP1340 simulation model is not known it is impossible to explain where that difference comes from.

TABLE 5. Comparison of simulated and measured results at rated load.

620 V	Simulated	Measured
Drain-source voltage, V	719	700
Peak current, A	2.04	1.85
Valley number	2	2
Switch. frequency, kHz	59.58	58.25
850 V	**Simulated**	**Measured**
Drain-source voltage, V	949	940
Peak current, A	2.07	1.75
Valley number	2	4
Switch. frequency, kHz	59,21	46.47

The measured "*switching-frequency vs. load*" curve is shown in Fig. 20 for the first time for a QRF with VSM. The maximum switching frequency was set to 67 kHz to make comparison with ACF in [7] plausible. In Fig. 20, at different loads and input voltages, the switching frequency was changing in the range from 41.9 kHz to 61.1 kHz. That range of variation is much higher than the ACF analyzed in [7]. Note that those results are read from the oscilloscope screen and might be prone to the measurement errors.

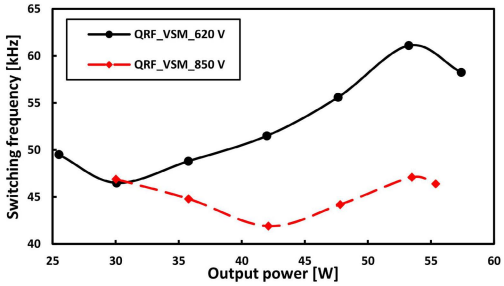

FIGURE 20. The measured "switching frequency vs. load" curves in VSM.

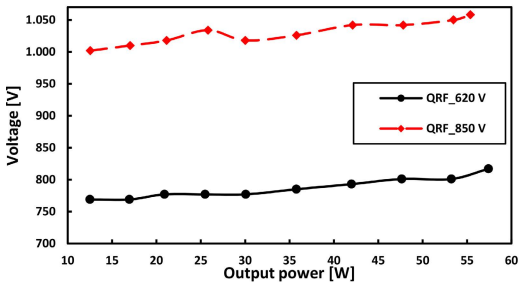

FIGURE 21. The measured "maximum drain-source voltage vs. load" in DCM and VSM.

In Fig. 21 the change of maximum Q drain-source voltage with load is presented. One can clearly see that this value is not constant and that is rises with increasing load—which makes sense due to higher stored energy in the leakage inductance. Those maximum values are not the clamped ones, but the first peak during the turn-off—which is on a side of safety. Hence designer shall take that into account during development. The voltage increase was 48 V (+7.7%) at 620 V and 56 V (+6.6%) at 850 V. Note that those results are read from the oscilloscope screen and might be prone to the measurement errors. In Fig. 21 for 850 V trace one can see transition between DCM and VSM around load of 30 W and that drain-source voltage is reduced a bit after transition to VSM—which is good and was expected.

B. OPERATION IN ICS STAND-BY MODE

As mentioned in sections II-C and III-B the ICS has a stand-by mode (i.e. no power-transfer) and an APS, in that case, has different input-voltage range (Table 2). That range is actually rectified three-phase ac grid-voltage. The expected

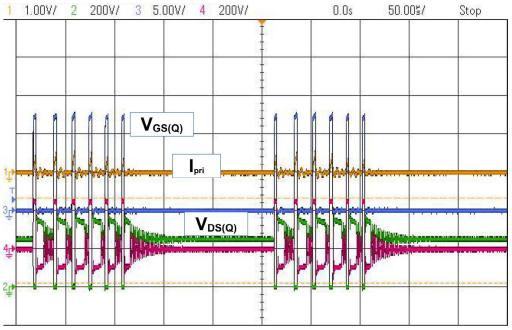

FIGURE 22. The QRF operating at 250 V dc input and 10 W load.

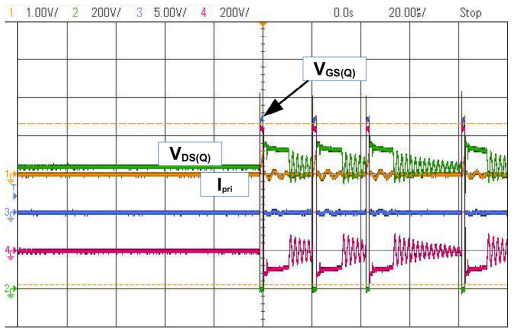

FIGURE 23. The QRF operating at 640 V dc input and 10 W load.

load of APS (i.e. QRF) is up to 10 W. Hence simulation and experimental results are done with that value. In this mode the 22 V output has only bleeder resistors as load, and others are having lower loads than in the ICS power-transfer mode.

The experimental waveforms of gate-source voltage, primary current and drain-source voltage (V_{DS}) at 250 V input and 10 W are shown in Fig. 22. There one can notice that the QRF is working in skip-mode. Similar behavior was noticed when operating at 640 V and 10 W (Fig. 23). Obviously, the total load of 10 W, with 22 V output unloaded, was not enough to force the NCP1340 into stable DCM, but always in the skip-mode. Discrepancy between simulated and experimental results cannot be explained since structure of the simulation model is not known to the user. Anyway, for this mode of operation this is not of major importance. The QRF was delivering load to the intended consumers reliably and that is what counts in practice. Note that tests are done with 250 V and not with the 240 V, as in simulations, because that is what we are expecting in our application.

The Fig. 24 shows measured QRF "*power losses vs. input voltage*". It was created out of measured input-power consumption, without load, then subtracting self-consumption and load on bleeder resistors. The QRF losses were predominant. Additionally, a trend-line (i.e. polynomial curve-fitting) is added to the graph showing (weak) quadratic dependency of QRF power losses vs. input voltage.

C. EFFICIENCY MEASUREMENTS

The efficiency measurements are provided in Fig. 25, Fig. 26, and Fig. 27 for the T3-1 transformer. The self-consumption of the primary side was estimated and considered. As expected,

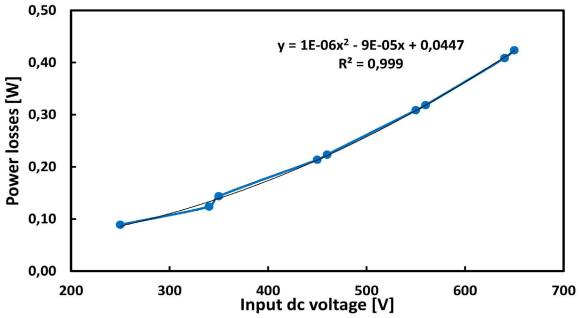

FIGURE 24. The QRF power losses vs. input dc voltage. Blue line: Microsoft® Excel® XY plot with smooth line. Black line: Microsoft® Excel® polynomial trend-line with its expression.

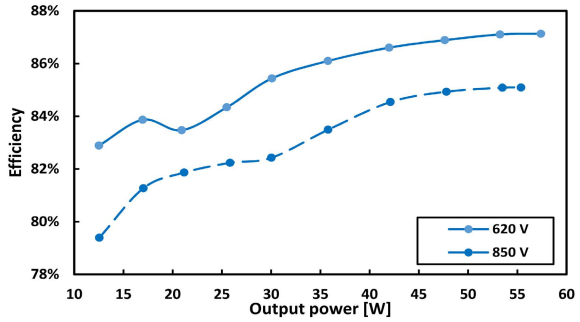

FIGURE 25. The QRF efficiency with T3-1 in ICS power-transfer mode.

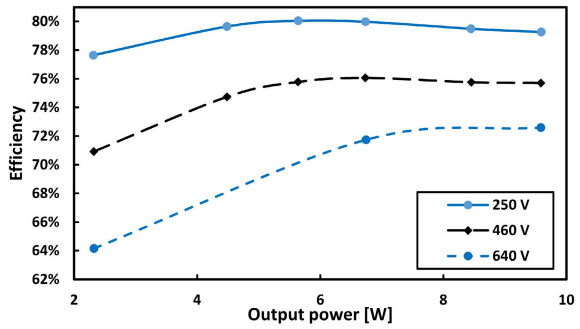

FIGURE 26. The QRF efficiency with T3-1 in ICS stand-by mode.

the efficiency at lower input voltage is higher due to lower switching losses. In Fig. 25 the maximum efficiencies of 87.1% at 620 V and 85.1% at 850 V inputs were achieved at 57.4 W and 55.4 W loads, respectively, in ICS power transfer mode. Those results are better than the ACF ones in [4] (see *Fig. 12* and *Fig. 26* there) and are comparable with other QRF in different application [14] (see *Fig. 12* there). The efficiencies in ICS stand-by mode are provided in Fig. 26. Also we see that they are higher than the ACF ones for the same application [4, Fig. 14].

In Fig. 27 dependency of efficiency vs. input dc voltage at a constant load is shown. There we can notice that, with voltage above 650 V, the graphs are almost linear and inverse-proportional to the input dc voltage—as expected. They are almost similar in shape to the equivalent plots for the 57 W

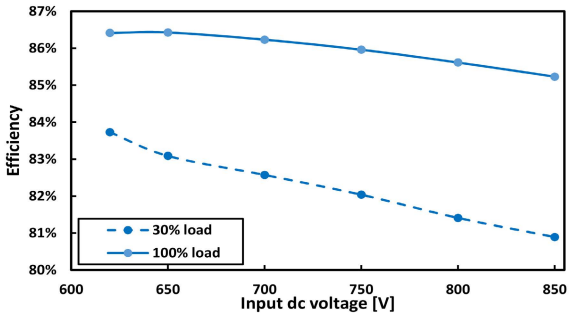

FIGURE 27. The QRF efficiency with const. loads and T3-1.

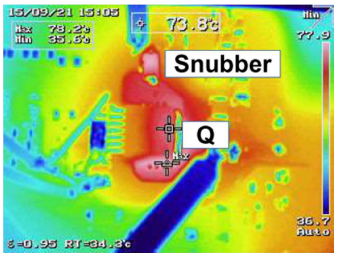

FIGURE 28. Thermal test of the QRF at 850 V and rated load.

ACF in [4, Fig.16]—only QRF has higher values as expected. Note that for this graph the regulation is done on the lowest-power output (6.75% of the total power) to make comparison to the ACF plausible. Also one can see that, at 30% load, the efficiency line is steeper than the 100% one. The reason is that, at smaller load, the switching and core losses, that are proportional to the input voltage, are more dominant than the other losses. Hence, those two efficiency lines are not parallel. The deviations in range 620–650 V are probably due to deviations in the switching-frequency change hence the QRF losses.

D. THERMAL TEST

The thermal test was done only on a bench demo-board at room temperature of approx. 25 °Cn. In Fig. 28 only 850 V results are shown because they are more severe. There we see that the power-switch Q has maximum temperature of 78.2 °Cn. The snubber diode has temperature close to the Q and it was expected that both parts will be the hottest ones. This result was acceptable. In other, non-documented measurements, it was noticed that temperatures of both were always ≤80 °Cn. Hence, cooling of any part was not needed—which was desired.

E. CONTROL ASPECTS

The compensator used was the ATL431 [38] based Type-2 one (dc gain, integrator, one pole and one zero) [37] with an optocoupler. Its generic form is shown in Fig. 29 [7] [37] and transfer function in (5). In Fig. 29 the V_{dd} is internal +5 V of the control IC, CTR is current-gain of optocoupler, and V_{out} is the Output 2 (Table 2). The compensator key-parameters were dc-gain of 31.9 dB, zero at 88 Hz, and pole at 3.67 kHz. During the design process and simulations, it was concluded

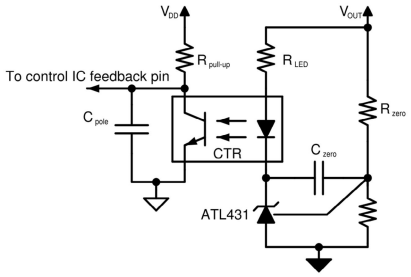

FIGURE 29. The generic Type-2 compensator with shunt regulator and an optocoupler.

TABLE 6. Comparison of bode plots at rated load.

620 V	Simulated	Measured
Bandwidth, Hz	643.5	235.7
Phase margin, °	76.2	77.3
Gain margin, dB	26	17
850 V	**Simulated**	**Measured**
Bandwidth, Hz	737.6	261
Phase margin, °	75.4	89
Gain margin, dB	25.9	14.8

that the compensator values cannot be the same as for the ACF from [4], [5], and [7].

The used optocoupler had minimum current-gain of 1.6 and its parasitic capacitance of 3.07 nF was estimated per method in [39]. Here, that method is improved a bit in a sense that optocoupler capacitance was calculated as an average of two measurements, at different operating points, thus improving accuracy of the result [7].

The transfer function of compensator from Fig. 29 is [7]

$$G(s) = -G_0 \cdot \frac{1 + \frac{\omega_z}{s}}{1 + \frac{s}{\omega_p}} \tag{5}$$

where G_0 is dc gain, ω_z zero angular frequency and ω_p pole angular frequency. The dc gain is calculated as [7], [37]

$$G_0 = CTR \cdot \frac{R_{pull-up}}{R_{LED}} \tag{6}$$

whereas zero and pole frequencies are calculated as [7], [37]

$$\omega_z = \frac{1}{R_{zero} \cdot C_{zero}};\ \omega_p = \frac{1}{R_{pull-up} \cdot C_{pole}}. \tag{7}$$

Note that C_{pole} represents parallel connection of external capacitor (if any) and optocoupler's (parasitic) capacitance [7].

1) BODE PLOTS

The Bode plots of QRF operating in VSM were measured with *Bode 100* vector network-analyzer [40]. Excitation signal was 50–60 mV (peak-to-peak). The regulated 5.5 V output was the Output 2 (Table 2). Measurements of Bode plots at 620 V and 850, with rated load, are shown in Fig. 30 and Fig. 31, respectively. Additionally, respective simulation results (Fig. 14) are included as well.

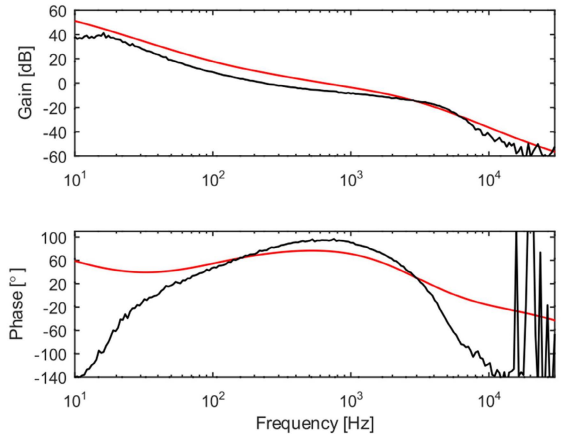

FIGURE 30. The simulated (red) and measured (black) Bode plots at 620 V and rated load with valley-switching.

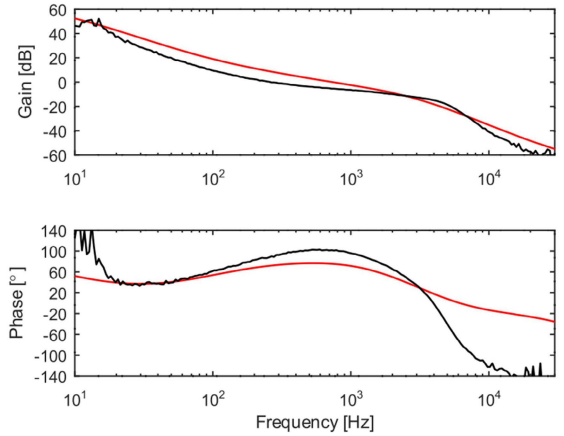

FIGURE 31. The simulated (red) and measured (black) Bode plots at 850 V and rated load with valley-switching.

The comparison of simulated and measured data is given in Table 6. There one can see significant discrepancy between the simulated and measured results for both input voltages. The reason for that might be because a generic QRF simulation model for the small-signal analysis was used. However, the designed converter was stable in whole input-voltage and load ranges with enough phase and gain margins. And that is what counts in practice at the end. The simulated results helped only to notice trends of change—which was helpful during design-phase to fine-tune the compensator. Similar approach was used in [7] as well.

In papers covering either small-signal modeling or compensator design of QRF the respective authors typically would present a few Bode diagrams, under key operating-conditions, and dynamic load-change in order to prove the effectiveness of their proposed methods. However, graphical representation of bandwidth (i.e. cross-over frequency; f_c), phase-margin (PM), and gain-margin (GM) changes in whole load-range was missing. Hence, in Fig. 32–Fig. 34 such graphs are presented for the first time in literature on the QRF with VSM.

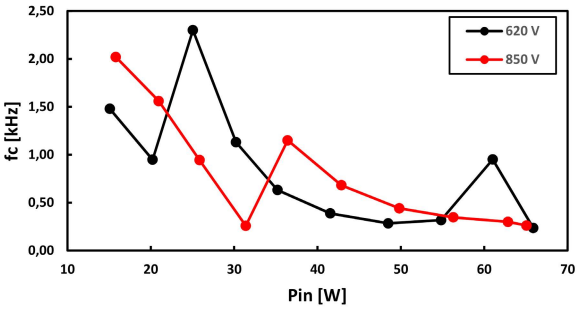

FIGURE 32. The QRF converter in VSM: bandwidth change with input voltage and input power.

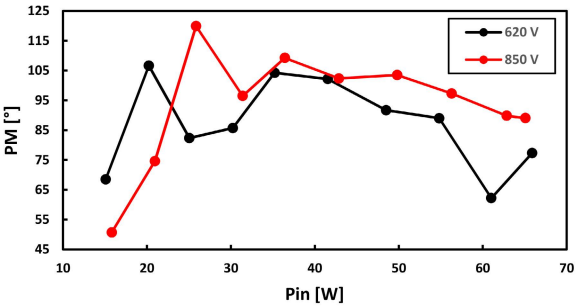

FIGURE 33. The QRF converter in VSM: phase-margin change with input voltage and input power.

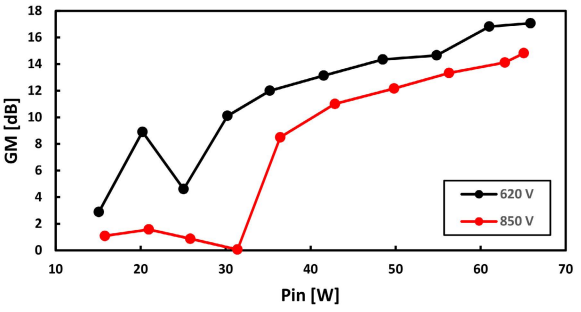

FIGURE 34. The QRF converter in VSM: gain-margin change with input voltage and input power.

From measured Bode plots, for each operating point, the f_c, PM, and GM are extracted. And results are plotted in Fig. 32–Fig. 34. Those quantities are plotted vs. input power because that was much faster to do rather than calculating output power by measuring load at five outputs. Operation at 10 loads and two input voltages were measured. Note that all taken Bode plots had first-order response that is typical for a peak-current controlled flyback dc-dc converter [37]. In Fig. 32–Fig. 34 one can see that all three quantities are changeable with load and input voltage—as expected. From practical experience, the PM shall be $>40°$ and GM>6 dB for all operating conditions. We see that the PM precondition is fulfilled everywhere, but the GM is achieved only for operation at input power higher than 35 W. However, in ICS power-transfer mode, the QRF will operate in VSM

because its input power will be always higher than 35 W. This means that no stability problems are expected. Additionally, the bandwidth was in 0.24–2.5 kHz range—which was wide (1:10 ratio between min and max), but still acceptable.

2) CROSS-REGULATION CHALLENGES

The analysis and mathematical modeling of cross-regulation effects with flyback converters is well covered in literature [41], [42]. In addition, some practical tips are given in [43] and [44]. This effect is unavoidable and depends on magnetizing inductance, leakage inductances of primary and secondary windings and clamp-voltage [42].

In this section we will elaborate practical cross-regulation behavior of our QRF with five outputs. In this design voltage fluctuations of the non-regulated outputs at light load were controlled by bleeder resistors (5 kΩ and 10 kΩ), Zener diodes (6 V, 16 V and 27 V), and stacked windings (Output 2 and Output 4 only) [43], [44]. The tests showed that satisfying results were achieved and that only the Zener diode 27 V was seldom activated. The same strategy was used with the ACF converters presented in [4], [5], and [7].

The regulated 5.5 V output was the Output 2 (Table 2) which had 13.75 W (24.1% of the total power). This was contrary to the common approach in practice of regulating the output with the highest power. In our case that was the 22 V one with 38.28 W (67.1% of the total power). The reasons for such an approach were different reference potentials and different loading of the outputs depending on the ICS operation modes. Similar approach was used with the ACF in [7] showing that the converter can be regulated with the smallest output as well.

In Fig. 35 and Fig. 36 the voltage changes are presented for QRF (T3-1) in VSM, i.e. ICS power-transfer mode. In Fig. 35 one can see that the regulated output has increasing static-error as its loading is increasing—which is still acceptable. In both figures we see that voltage fluctuations of non-regulated outputs are acceptable, i.e. within allowed limits without reaching thresholds of Zener diodes. That also depends in which sequence one loads the respective outputs, and, in our case, that was chosen in accordance with expected behavior of the ICS.

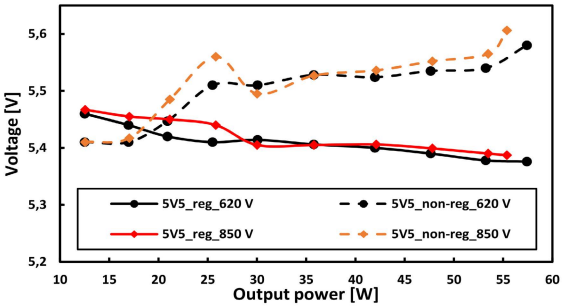

FIGURE 35. The regulated 5.5 V output (solid lines) and non-regulated 5.5 V output (dashed lines) for QRF in VSM at 620 V (black) and at 850 V (red).

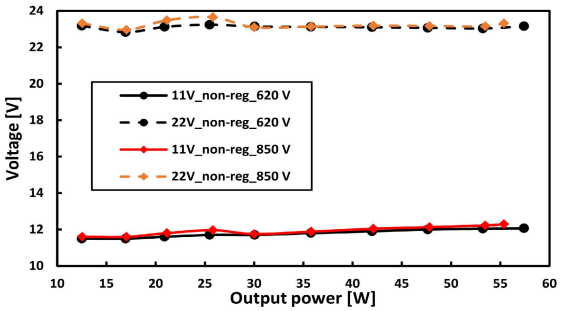

FIGURE 36. The non-regulated outputs 11 V (solid lines) and 22 V (dashed lines) for QRF in VSM at 620 V (black) and at 850 V (red).

The voltage changes at QRF outputs when the ICS is stand-by mode are shown in Fig. 37 and Fig. 38. There we can see that voltage fluctuations of non-regulated outputs are acceptable, i.e. within allowed limits. And at only two points (>6.7 W) voltage of the 22 V output reached the threshold of respective Zener diode (27 V). In Fig. 37 and Fig. 38 the QRF was operating in the skip-mode (see section IV-B as well).

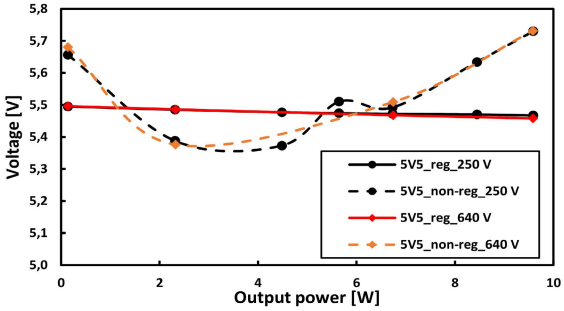

FIGURE 37. The regulated 5.5 V output (solid lines) and non-regulated 5.5 V output (dashed lines) for QRF in skip-mode at 250 V (black) and at 640 V (red).

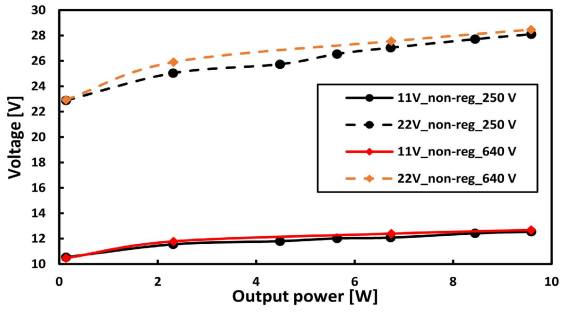

FIGURE 38. The non-regulated outputs 11 V (solid lines) and 22 V (dashed lines) for QRF in skip-mode at 250 V (black) and at 640 V (red).

3) INFLUENCE OF CONTROL-STRATEGY ON THE QRF EFFICIENCY

During experiments it was noticed that the efficiency of multi-mode QRF with variable switching frequency also depends on the designed compensator and chosen regulated output. The reason for it is that both items influence internal logic

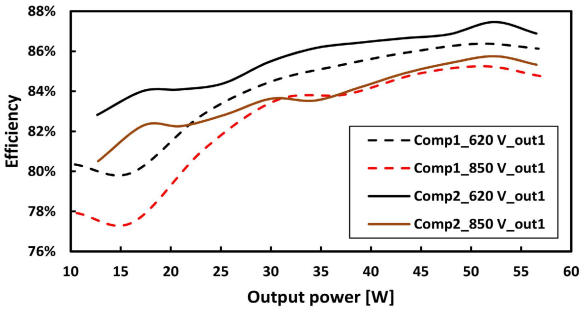

FIGURE 39. The 57 W QRF efficiency with two different compensators.

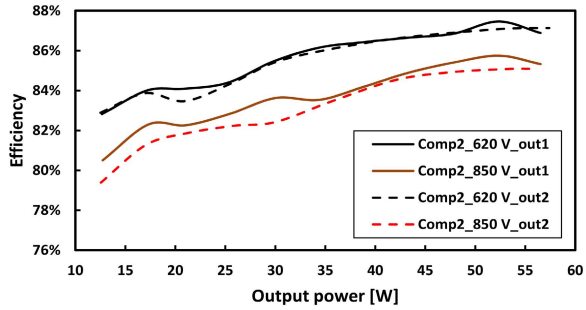

FIGURE 40. The 57 W QRF efficiency with regulation on two different 5.5 V outputs having the same compensator.

of the control IC (i.e. NCP1340) which then reflects on the value of switching frequency. The representative examples are given in Fig. 39 and Fig. 40. The outputs out1 and out2 are related to Output 1 and Output 2 in the Table 2, respectively.

In Fig. 39 the only difference in compensators was that the zeros were different 10 times between each other (e.g., *Comp1*: 8.84 Hz; *Comp2*: 88.4 Hz). And regulation was done on Output 1 (3.85 W or 6.7% of the total power). There one can see that zero-placement plays important role not only on converter dynamic behaviour, but on the efficiency as well. In Fig. 40 the same compensator (*Comp2*) was used for regulation on Output 1 and Output 2. Unexpectedly, one can see that QRF efficiency is a bit higher when regulation is done on smallest output (out1). But, in Fig. 40 the difference in efficiency, due to different outputs, was much smaller when compared with Fig. 39 and contribution of zero-placement there.

4) DYNAMIC LOAD-CHANGE

The performance of designed compensator is also verified by applying dynamic load-change on the regulated output 5.5 V (Table 2). The scope screenshots of operation at 620 V are provided in Fig. 41 and Fig. 42. In both cases the non-regulated output had constant load of 0.7 À and 22 V has 1 A load. The load currents were changed from 1 A to 2 A (Fig. 41) and vice versa (Fig. 42). At 1 A the QRF was operating in 6th valley and with 2 A the QRF was operating with 4th valley. The reason for those load-current values is that they were realistic to expect in the real application. Note that simulations (Fig. 15 and Fig. 16) are done for more severe

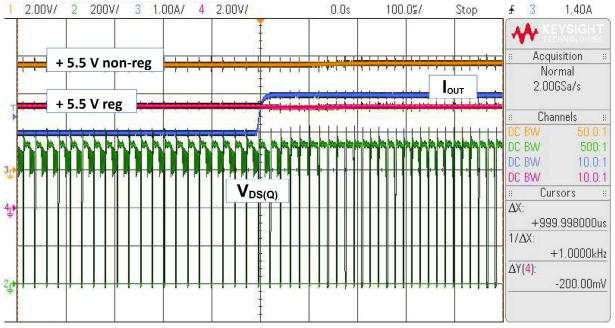

FIGURE 41. The 57 W QRF with dynamic load-change at the regulated 5.5 V output. Load change: 1 A to 2 A.

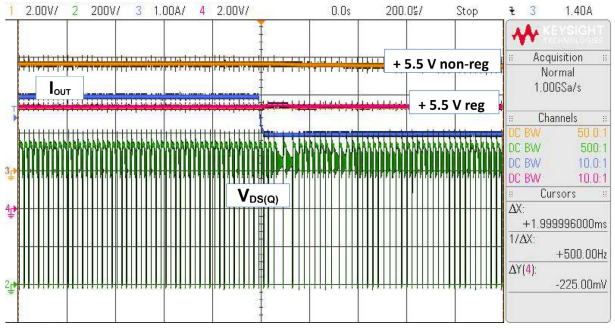

FIGURE 42. The 57 W QRF with dynamic load-change at the regulated 5.5 V output. Load change: 2 A to 1 A.

cases (0.5 A to 2.5 A, and vice versa) just to see how the regulator behaves. In Fig. 41 can be seen that the undershoot was −200 mV, and from Fig. 42 we see that the overshoot was +225 mV—which was very good and that proves good design of the compensator.

Similar experiments are done at 850 V and results were similar—except that operating valleys were 5th and 6th. Hence, the 850 V screenshots are not included here.

5) POWER TRANSITION-THRESHOLD TO VALLEY-SWITCHING MODE

During experiments it was noticed that transition-thresholds between DCM and VSM vary with input voltage, load and that it depends on the output on which regulation happens. It was possible to identify input-powers at which transition happens so that end user can get a feeling about it. In the experiments the QRF load was always increasing for all input voltages, i.e., hysteresis effect was not considered.

The resulting graph is shown in Fig. 43. There one can see that dotted areas (red or black) represent areas where QRF operates in VSM starting from the 6th valley—except for the Output 1 at 620 V where it started from 7th valley. We see also that, if regulation happens at output with higher load (i.e. Output 2; *Out2_REG* in Fig. 43) then QRF earlier enters the VSM—which is more desired. Those transitions can be seen in Fig. 32–Fig. 34 as well. This topic will be further investigated in a future study.

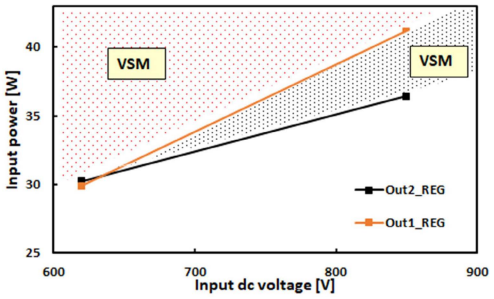

FIGURE 43. QRF transition thresholds to the valley-switching mode.

F. COMPARISON TO AN ACF CONVERTER

The QRF had the same secondary sides, primary switch [32] and transformer as the ACF presented in [4], [5], and [7]. This made comparison to ACF easier and more plausible. In [4] was shown that the 57 W QRF has higher efficiency in whole load range, is ≈23% cheaper, and occupies ≈11% less board-space than the 57 W ACF in the same application.

Subject of this section is comparison of QRF Bode plots versus ACF converter [4, Figs. 20 and 22]. Note that the Bode plots for ACF were given when it was operating in active-clamping mode (ACM). In order to make such comparison plausible the QRF had regulation at the Output 1 (3.85 W, Table 2) and used the same compensator as the ACF in [4], [7] (i.e. having zero at 8.84 Hz). Here, in section E-3) that compensator was named *Comp1*. From Bode plots, for each measured point, the bandwidth, PM, and GM were extracted. The results are plotted in Fig. 44, Fig. 45, and Fig. 46. Those quantities are plotted vs. input power because that was easier to do. Operation at 10 loads and two input voltages were measured. From Fig. 44–Fig. 46 we see that the QRF in VSM (i.e. ICS power-transfer mode) has lower bandwidth than the ACF in ACM—which resulted in higher PM and GM. Also, it is noticeable that the QRF power transition-thresholds from DCM to VSM were in the input-power range from 35 W (at 620 V) to 41 W (at 850 V).

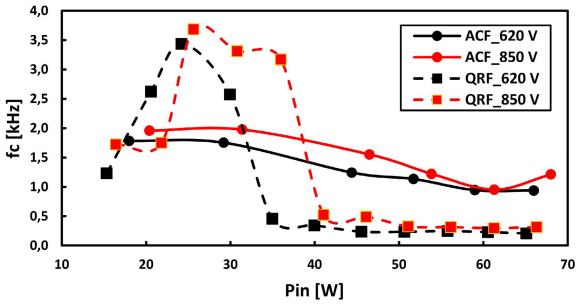

FIGURE 44. QRF vs. ACF: comparisons of the bandwidths.

From this section, [4] and [7] we can conclude that, for the same specification, the conventional DCM flyback, ACF or QRF VSM dc-dc converters may be stabilized with the Type-2 compensator (dc gain, integrator, one pole and one zero) only, but they must have different parameters (e.g. at least position of a zero shall be different).

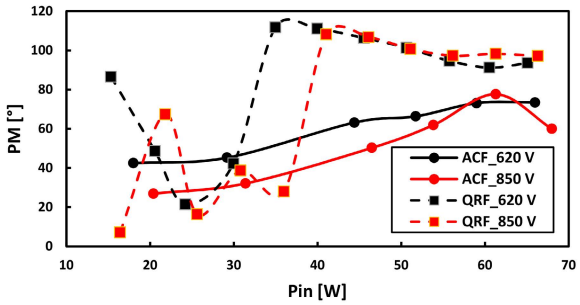

FIGURE 45. QRF vs. ACF: comparisons of the PM.

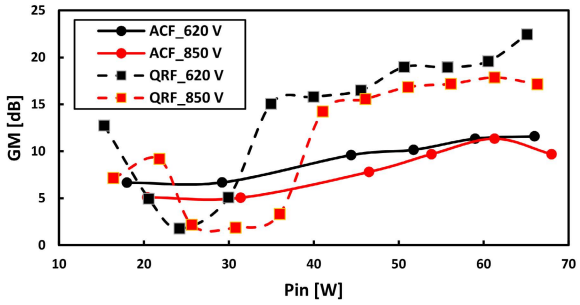

FIGURE 46. QRF vs. ACF: comparisons of the GM.

V. SUMMARY AND CONCLUSIONS

This paper presented investigation of QRF with VSM dc-dc converter 57 W used as APS of an ICS for BEV. Since the QRF was supplied from HDCIV that created additional challenges for its design which are different from mainstream QRF applications. However, findings and conclusions are valid for any QRF converter and some of them are even valid for any flyback converter. The statements "…*for the first time*" were related to the reported results or findings on QRF with valley switching—not to the methods of achieving it. The original or novel results and analysis related to 12 figures (Figs. 20, 21, 24, 32, 33, 34, 39, 40, 43, 44, 45, and 46) were never presented before for any QRF which was ensured by checking >70 papers on the topic.

First, an overview of the QRF control ICs is given with suggestions of control IC's features for future products. Attention was given to power-supply architecture of such systems. The converter and transformer data were presented with ICS specific challenges. The OPP was covered as well.

The simulated and experimental results of voltage and current waveforms had some acceptable deviations. Although simulated and measured Bode plots were not matched, the simulations were good enough to help design a good compensator. As a result the designed QRF was stable in whole load and input-voltage range. And that is what matters in practice. This was verified by dynamic load-change tests.

Thermal tests showed that additional cooling of switch or any other component was not needed because maximum temperatures were always below 80 °C. The maximum efficiency of 87.1% was achieved at 620 V input.

Also, the "*switching frequency vs. load*" curves were included as well as "*maximum drain-source voltage of Q vs. load*". This improved understanding of the QRF operation with variable switching-frequency. The QRF regulation on outputs with 6.7% and 24.1% of the total power—contrary to the common approach by regulating the biggest one—was proven to be feasible. It was also shown that for a multi-mode QRF, with variable switching-frequency, choice of the compensator's zero and the regulated output has influence on its efficiency.

Bode plots are measured for two input-voltages at 10 different loads. Then f_C, PM, and GM were extracted and plotted versus input-power—for the first time. They were changeable with input-voltage and load as expected. Also it was shown that only with the Type-2 compensator is possible to control such QRF.

At the end, the f_C, PM, and GM changes were compared between QRF and ACF. It was shown that those converters, for the same specification, cannot share the same compensator. And that the difference must be at least in placement of a zero.

In general, it seems that the QRF dc-dc converter in VSM is still better alternative to an ACF dc-dc converter in 800 V ICS application considering price, occupied board-space, simplicity, cooling needs, and efficiency. However, for final judgement about these two converters, two areas would need further investigations:

- Stability of transition thresholds between DCM and VSM modes when load is increasing and decreasing, and comparing it with the equivalent transitions (DCM-ACM) by ACF [7];
- Comparison of electromagnetic interferences (EMI) between QRF and ACF in ICS application.

Limitations of this study are:

- Because off-the-shelf control IC was used there was no freedom in the control method.
- Since this work was part of a commercial project, the project-timeline had higher priority over applied-research activities and not all data could have been revealed. Also, there was no time for complicated mathematics or for development of dedicated optimization algorithms. Hence, sometimes one had to use trial-and-error approach to find a good-enough solution and move-on.
- Some of the formulas are derived by curve-fitting of the experimental curves.

Focus of the future work will be on, above mentioned, areas for further investigation as well as trying to reduce high ratio between min and max values of bandwidth. Additional areas to work on are mathematical modelling of Bode plots' differences between ACF and QRF converters, analysis of cross-regulation effects depending on the regulated output, development of mathematical expressions for curves derived by curve-fitting, and inclusion of their error-analysis.

VI. CONFLICT OF INTEREST DECLARATION

Author declare no conflict of interests that could have influenced the work reported in this paper and do not endorse any manufacturer of electronics components.

ACKNOWLEDGMENT

The author would like to thank Brusa Elektronik (München) GmbH, especially T. Burgstaller and Dr. A. Boulous; ex-colleague Dr. M. Pavlovsky; Dr. M. Khalilian, and other colleagues. He also thanks United Silicon Carbide Inc. for providing samples of the 1700 V SiC FETs and to transformer-suppliers who provided many custom-designed parts so far. Special thanks goes to his mentor Prof. P. Pejović, School of Electrical Enginering, University of Belgrade, Serbia, for overall unconditional support during his Ph.D. study.

Some of the figures were made or edited by using *FidoCADJ* [45], *GNU Octave* [46], and *Libre Office Draw* [47]. The references were managed in Zotero [48].

REFERENCES

[1] IEA, Paris. (May 2022). *The Global EV Outlook 2022*. Accessed: Jun. 6, 2022. [Online]. Available: https://www.iea.org/reports/global-ev-outlook-2022

[2] A. Mahesh, B. Chokkalingam, and L. Mihet-Popa, "Inductive wireless power transfer charging for electric vehicles—A review," *IEEE Access*, vol. 9, pp. 137667–137713, 2021, doi: 10.1109/ACCESS.2021.3116678.

[3] Market Research Report. Wireless Charging Market for Electric Vehicles. MARKETSANDMARKETS. Accessed: Jun. 6, 2022. [Online]. Available: https://www.marketsandmarkets.com/Market-Reports/wireless-ev-charging-market-170963517.html

[4] D. Vračar and P. Pejović, "Active-clamp flyback converter as auxiliary power-supply of an 800 V inductive-charging system for electric vehicles," *IEEE Access*, vol. 10, pp. 38254–38271, 2022, doi: 10.1109/ACCESS.2022.3165059.

[5] D. Vračar and M. Pavlovskć, "Implementation of active-clamped flyback DC–DC converter in an 800 V system," in *Proc. Int. Exhib. Conf. Power Electron., Intell. Motion, Renew. Energy Energy Manag.*, 2021, pp. 1163–1170. [Online]. Available: https://ieeexplore.ieee.org/document/9472384

[6] D. Vračar, M. Pavlovský, and P. Pejović, "Active-clamped flyback DC–DC converter in three-phase application," in *Proc. 21st Int. Symp. Power Electron. (Ee)*, Novi Sad, Serbia, Oct. 2021, pp. 1–6, doi: 10.1109/Ee53374.2021.9628263.

[7] D. Vračar and P. Pejović, "Active-clamped flyback DC–DC converter in an 800 V application: Design notes and control aspects," *J. Electr. Eng.*, vol. 73, no. 4, pp. 237–247, 2022, doi: 10.2478/jee-2022-0032.

[8] *IEC Standard Voltages*, document IEC 60038:2009+AMD1:2021 CSV, 2021.

[9] *Regulation No 100 of the Economic Commission for Europe of the United Nations (UNECE)—Uniform Provisions Concerning the Approval of Vehicles With Regard to Specific Requirements for the Electric Power Train [2015/505]*. UNECE, document ECE R 100, 2015.

[10] M. T. Zhang, M. M. Jovanovic, and F. C. Y. Lee, "Design considerations and performance evaluations of synchronous rectification in flyback converters," *IEEE Trans. Power Electron.*, vol. 13, no. 3, pp. 538–546, May 1998, doi: 10.1109/63.668117.

[11] Y. Panov and M. M. Jovanovic, "Adaptive off-time control for variable-frequency, soft-switched flyback converter at light loads," in *Proc. 30th Annu. IEEE Power Electron. Spec. Conf. Record.*, Charleston, SC, USA, vol. 1, 1999, pp. 457–462, doi: 10.1109/PESC.1999.789046.

[12] G. Mauromicale, A. Raciti, S. A. Rizzo, G. Susinni, F. Fusillo, A. Palermo, F. Scrimizzi, and R. Scollo "Si and GaN devices in quasi resonant flyback converters for wall charger applications," in *Proc. IEEE Energy Convers. Congr. Exposit. (ECCE)*, Baltimore, MD, USA, Sep. 2019, pp. 3253–3258, doi: 10.1109/ECCE.2019.8912178.

[13] J. C. D. Manzano, R. M. Montaril, A. H. Ballado, M. A. Lopez, J. M. Martinez, and F. L. Valiente, "Housekeeping and auxiliary quasi-resonant flyback converter design for a 350 W power supply," in *Proc. IEEE 12th Int. Conf. Humanoid, Nanotechnol., Inf. Technol., Commun. Control, Environ., Manag. (HNICEM)*, Manila, Philippines, Dec. 2020, pp. 1–6, doi: 10.1109/HNICEM51456.2020.9400056.

[14] Y. Mo, H. Qin, W. Chen, Y. Yang, S. Wang, L. Hu, and L. Xie "Auxiliary power supply with SiC MOSFET for wide-range high voltage input applications," in *Proc. IEEE 9th Int. Power Electron. Motion Control Conf. (IPEMC-ECCE Asia)*, Nanjing, China, Nov. 2020, pp. 137–141, doi: 10.1109/IPEMC-ECCEAsia48364.2020.9368165.

[15] Y. Sahin and G. Tohumoglu, "Quasi resonant flyback topology based LCD TV power supply board design and power loss analysis," in *Proc. 2nd Eur. Conf. Elect. Eng. Comput. Sci. (EECS)*, Bern, Switzerland, Dec. 2018, pp. 16–20, doi: 10.1109/EECS.2018.00012.

[16] H. Onay and V. Süel, "A comprehensive loss analysis of quasi resonant flyback converter for design purpose," in *Proc. Int. Exhib. Conf. Power Electron., Intell. Motion, Renew. Energy Energy Manag.*, Shanghai, China, 2018, pp. 193–200. [Online]. Available: https://ieeexplore.ieee.org/document/8470536

[17] Y. Panov and M. M. Jovanovic, "Adaptive off-time control for variable-frequency, soft-switched flyback converter at light loads," *IEEE Trans. Power Electron.*, vol. 17, no. 4, pp. 596–603, Jul. 2002, doi: 10.1109/TPEL.2002.800958.

[18] Y.-B. Park and H.-S. Choi, "A hybrid control method to maximize efficiency for active mode efficiency regulation," in *Proc. 29th Int. Telecommun. Energy Conf.*, Rome, Italy, 2007, pp. 83–88, doi: 10.1109/INTLEC.2007.4448743.

[19] R. D. Stracquadaini, "Mixed mode control (fixed off time & quasi resonant) for flyback converter," in *Proc. 36th Annu. Conf. IEEE Ind. Electron. Soc.*, Glendale, AZ, USA, Nov. 2010, pp. 556–561, doi: 10.1109/IECON.2010.5675222.

[20] J. Park, Y.-J. Moon, M.-G. Jeong, J.-G. Kang, S.-H. Kim, J.-C. Gong, and C. Yoo, "Quasi-resonant (QR) controller with adaptive switching frequency reduction scheme for flyback converter," *IEEE Trans. Ind. Electron.*, vol. 63, no. 6, pp. 3571–3581, Jun. 2016, doi: 10.1109/TIE.2016.2523931.

[21] Q. Wu, X. Li, Y. Han, Z. Di, and Q. Feng, "A valley-locking control scheme for an audible noise-free valley-skip-mode flyback converter," *IEEE Trans. Ind. Electron.*, vol. 69, no. 7, pp. 7285–7294, Jul. 2022, doi: 10.1109/TIE.2021.3099223.

[22] J. Zhang, H. Zeng, and X. Wu, "An adaptive blanking time control scheme for an audible noise-free quasi-resonant flyback converter," *IEEE Trans. Power Electron.*, vol. 26, no. 10, pp. 2735–2742, Oct. 2011, doi: 10.1109/TPEL.2011.2114675.

[23] Datasheet. (Mar. 2021). NCP1340: Quasi-Resonant Controller, High-Voltage, Featuring Valley Lock-Out Switching. Onsemi. Accessed: May 8, 2022. [Online]. Available: https://www.onsemi.com/pdf/datasheet/ncp1340-d.pdf

[24] *SIMetrix/SIMPLIS Ver. 9—Advanced Power System Simulation*, Software (Commercial), Simplis Technologies Inc., Portland, OR, USA, 2022.

[25] Datasheet. (Aug. 2015). UCC28600 8-Pin Quasi-Resonant Flyback Green-Mode Controller. Texas Instruments. Accessed: Jun. 6, 2022. [Online]. Available: https://www.ti.com/lit/gpn/ucc28600

[26] Datasheet. (Apr. 2012). L6566BH Multi-Mode Controller for SMPS. STMicroelectronics. Accessed: Jun. 6, 2022. [Online]. Available: https://www.st.com/resource/en/datasheet/l6566bh.pdf

[27] Datasheet. (Feb. 2022). InnoSwitch3-EP Family. Power Integrations. Accessed: Jun. 6, 2022. [Online]. Available: https://www.power.com

[28] *Electromagnetic Compatibility (EMC)—Part 4-5: Testing and Measurement Techniques—Surge Immunity Test*, document IEC 61000-4-5:2014+AMD1:2017 CSV, Aug. 2017.

[29] Application Note. (Jul. 2014). Designing a Quasi-Resonant Adaptor Driven by the NCP1339. Onsemi. Accessed: May 8, 2022. [Online]. Available: https://www.onsemi.com/pub/collateral/and9176-d.pdf

[30] Application Note. (Dec. 2009). Designing a Quasi-Resonant Adaptor Driven by the NCP1380. Onsemi. Accessed: May 8, 2022. [Online]. Available: https://www.onsemi.com/pub/collateral/and8431-d.pdf

[31] C. Adragna. (Nov. 2002). AN1326: L6565 Quasi-Resonant Controller. STMicroelectronics. Accessed: Jun. 6, 2022. [Online]. Available: https://www.st.com

[32] Datasheet (Preliminary). (Oct. 2019). UF3C170400B7S, 1700 V, SiC FET. UnitedSiC. Accessed: May 22, 2022. [Online]. Available: https://www. sales@unitedsic.com

[33] A. Ayachit, A. Reatti, and M. K. Kazimierczuk, "Magnetising inductance of multiple-output flyback DC–DC convertor for discontinuous-conduction mode," *IET Power Electron.*, vol. 10, no. 4, pp. 451–461, Mar. 2017, doi: 10.1049/iet-pel.2016.0390.

[34] *Safety of Transformers, Reactors, Power Supply Units and Combinations Thereof—Part 1: General Requirements and Tests*, document IEC 61558-1:2017, 2017

[35] *Safety of Transformers, Reactors, Power Supply Units and Combinations Thereof—Part 2–16: Particular Requirements and Tests for Switch Mode Power Supply Units and Transformers for Switch Mode Power Supply Units for General Applications*, document IEC 61558-2-16:2021, 2021.

[36] C. Basso, *Transfer Functions of Switching Converters*, 1st ed. AZ, USA: Faraday Press, 2021.

[37] C. Basso, *Switch-Mode Power Supplies: Spice Simulations and Practical Designs*, 2nd ed. New York, NY, USA: McGraw-Hill Professional, 2014.

[38] Datasheet. (Oct. 2016). ATL431, ATL432 2.5-V Low Iq Adjustable Precision Shunt Regulator. Texas Instruments. Accessed: Mar. 19, 2022. [Online]. Available: https://www.ti.com/lit/gpn/atl431

[39] (Jan. 3, 2018). *How to measure the Frequency Response of an Opto-Isolator for Power Supply Applications*, Accessed: Aug. 31, 2021. [Online]. Available: https://www.youtube.com/watch?v=Eq8hGJ2ZLac

[40] Quick Start Guide. (2019). Bode 100 Vector Network Anlyzer. OMICRON Lab. Accessed: May 22, 2022. [Online]. Available: https://www.omicron-lab.com

[41] D. Maksimovi? and R. Erickson, "Modeling of cross-regulation in multiple-output flyback converters," in *Proc. 14th Annu. Appl. Power Electron. Conf. Expo. Conf.*, Dallas, TX, USA, vol. 2, 1999, pp. 1066–1072, doi: 10.1109/APEC.1999.750501.

[42] C. Ji, M. Smith, K. M. Smedley, and K. King, "Cross regulation in flyback converters: Analytic model and solution," *IEEE Trans. Power Electron.*, vol. 16, no. 2, pp. 231–239, Mar. 2001, doi: 10.1109/63.911147.

[43] Tutorial. (Oct. 2008). Multi-Output Flyback Off-Line Power Supply. Onsemi. Accessed: May 27, 2022. [Online]. Available: https://www.onsemi.com/pub/collateral/tnd351-d.pdf

[44] C. Mullett and F. Cathell, "Improving the regulation of multi-output flyback converters," in *Proc. 24th Annu. IEEE Appl. Power Electron. Conf. Exposit.*, Washington, DC, USA, Feb. 2009, pp. 1923–1926, doi: 10.1109/APEC.2009.4802935.

[45] *FidoCadJ—A Free Graphical Editor for Electronics, Ver. 0.2.47*, Software (Free), Boston, MA, USA, 2021.

[46] *GNU Octave—A High-Level Interactive Language for Numerical Computations, Ver. 6.2.0*, Software (Free), Boston, MA, USA, 2021.

[47] Software (Free). (2021). *Libre Office Draw, Ver. 6.2.5.x*. Accessed: Feb. 28, 2022. [Online]. Available: https://www.libreoffice.org

[48] *Zotero Ver. 6.0.x*, Software (Free), Corporation for Digital Scholarship, Vienna, VA, USA, Apr. 2022.

DARKO Đ. VRAČAR (Member, IEEE) received the Dipl.-Ing. and Magister degrees in electrical engineering from the School of Electrical Engineering, University of Belgrade, Serbia, in 2000 and 2007, respectively, where he is currently pursuing the Ph.D. degree in power converters and drives.

He is also a Senior Staff Engineer with BRUSA Elektronik (München) GmbH, Munich, Germany. He has 21 years of industrial experience. Some areas of expertise are implementation of telecom and datacenter power supplies, and research and development of power electronics' systems, such as solar inverters, SMPS for industrial and automotive applications. He has published several articles related to power converters and drives and holds one patent in power conversion systems. In addition, he was delivering training sessions related to power electronics or industrial standards. His research interests include simulation, control, and design of power converters. He is a member of the following IEEE Societies: Industry Applications, Industrial Electronics, Power Electronics, and Circuits and Systems. He is a Reviewer of journal *Electronics*.